





Determining the Thermal Conductivity of Gehlenite by Thermal Microscopy at Room Temperature

Yuta Inoue¹ · Takashi Watanabe¹ · Miyuki Hayashi¹  · Masahiro Susa¹ · Rie Endo^{1,2} 

Received: 19 January 2023 / Accepted: 4 March 2023 / Published online: 26 April 2023
© The Author(s) 2023

Abstract

The thermal conductivity of a single-phase gehlenite ($2\text{CaO Al}_2\text{O}_3 \text{ SiO}_2$) sample was determined using thermal microscopy. The composition of the primary crystal region of the gehlenite sample was $\text{CaO: SiO}_2\text{:Al}_2\text{O}_3 = 38\text{:}28\text{:}34$ (mass%), which was maintained after melting and cooling. After polishing the samples, the size of the gehlenite crystal was sufficiently large to be measured using a thermal microscope. The value of $\sqrt{\lambda C \rho}$, where λ is thermal conductivity C is specific heat and ρ is density, of the samples was measured every $10 \mu\text{m}$ to obtain its distribution. When comparing the results with the optical microscopy image of the sample, the gehlenite region showed a larger value of $\sqrt{\lambda C \rho}$ than the glassy region. Specifically, the value of $\sqrt{\lambda C \rho}$ of the gehlenite region was determined to be $2.2 \pm 0.1 \text{ kJs}^{-0.5} \cdot \text{m}^{-2} \cdot \text{K}^{-1}$, which resulted in a thermal conductivity of $2.1 \pm 0.2 \text{ Wm}^{-1} \cdot \text{K}^{-1}$. Moreover, the oxide gehlenite phase showed lower thermal conductivity than the other constituent phases, i.e., CaO , Al_2O_3 , and SiO_2 .

Keywords Gehlenite · Single-phase crystal · Thermal conductivity · Thermal effusivity · Thermal inertia · Thermal microscopy

1 Introduction

Gehlenite ($2\text{CaO Al}_2\text{O}_3 \text{ SiO}_2$) is a constituent melilite substance and is sometimes formed during steelmaking processes, such as in the continuous casting process for high-aluminum steel production. The flux between the molten steel and the mold regulates the heat removal rate from the steel product, prevents re-oxidation of steel,

✉ Rie Endo
rie-endo@shibaura-it.ac.jp

¹ Department of Materials Science and Engineering, Tokyo Institute of Technology, Meguro-Ku, Tokyo 152-8550, Japan

² Department of Materials Science and Engineering, Shibaura Institute of Technology, Koto-Ku, Tokyo 135-8548, Japan

and controls the lubrication between the steel and the mold. Mild cooling has been considered a promising approach for producing defect-free steel. The composition of the mold flux is generally designed to crystallize cuspidine [1–15] since the strong radiation light from the molten steel is scattered by the crystal grains, reducing the radiative heat flux in the process [16] to achieve mild cooling. However, in the case of Al-killed steels, which contain high concentrations of Al, gehlenite is usually formed in the flux owing to the reduction of SiO_2 in the mold flux by Al in the steel [17–20]. Because gehlenite has a high melting point, it preferentially crystallizes, unlike the mold flux design, and reduces its fluidity, which may result in the loss of lubricity [21–26]. However, there are no reports on controlling the heat removal rate of steel when gehlenite crystallizes.

Controlling the heat removal rate requires simulations based on the thermophysical properties of the mold flux, steel, mold, etc. However, the thermal conductivity of the crystalline phase of gehlenite, which is essential as input data, has only been reported for sintered materials [27, 28]. Steadman et al. [27] reported the thermal conductivity of sintered dense gehlenite containing impurities such as Fe_2O_3 , Na_2O , etc. Jia et al. reported [28] for porous gehlenite. The high porosity of the sample prevents the estimation of the thermal conductivity of gehlenite. It is considered that the high melting point and faceted structure of gehlenite hinder the preparation of single-phase samples to measure thermal conductivity.

Recently, the thermoreflectance method was developed to measure the value of $\sqrt{\lambda C \rho}$, where λ is thermal conductivity C is specific heat and ρ is density, of a small area [29–34]. The value of $\sqrt{\lambda C \rho}$ is often called thermal effusivity or thermal inertia; hereafter, $\sqrt{\lambda C \rho}$ is expressed with b . The thermoreflectance method heats the sample surface with a laser (pump laser), and the temperature change in the sample surface is measured as the intensity change in the reflected laser (probe laser) [29]. Based on the thermoreflectance technique, a thermal microscope uses a probe laser with a diameter of a few micrometers. This technique enables the measurement of the value of b of samples on the order of $10 \mu\text{m}$ [30]. The distribution of value of b can be obtained by using a micrometer that automatically moves the stage in the X – Y direction. Because of the above, this study aimed to determine the thermal conductivity of gehlenite through the measurement of the value of b of gehlenite at room temperature using a thermal microscope.

2 Experimental Section

In this study, a sample of single-phase crystallized gehlenite was prepared to coexist with a glass, and a thermal microscope was used to measure its value of b .

2.1 Sample Preparation and Analysis

To ensure that the primary crystal phase of the samples was single-phase gehlenite, the chemical composition implemented was 38CaO – $28\text{Al}_2\text{O}_3$ – 34SiO_2 (in mass%). Figure 1 plots the sample composition on a CaO – SiO_2 – Al_2O_3 ternary phase diagram

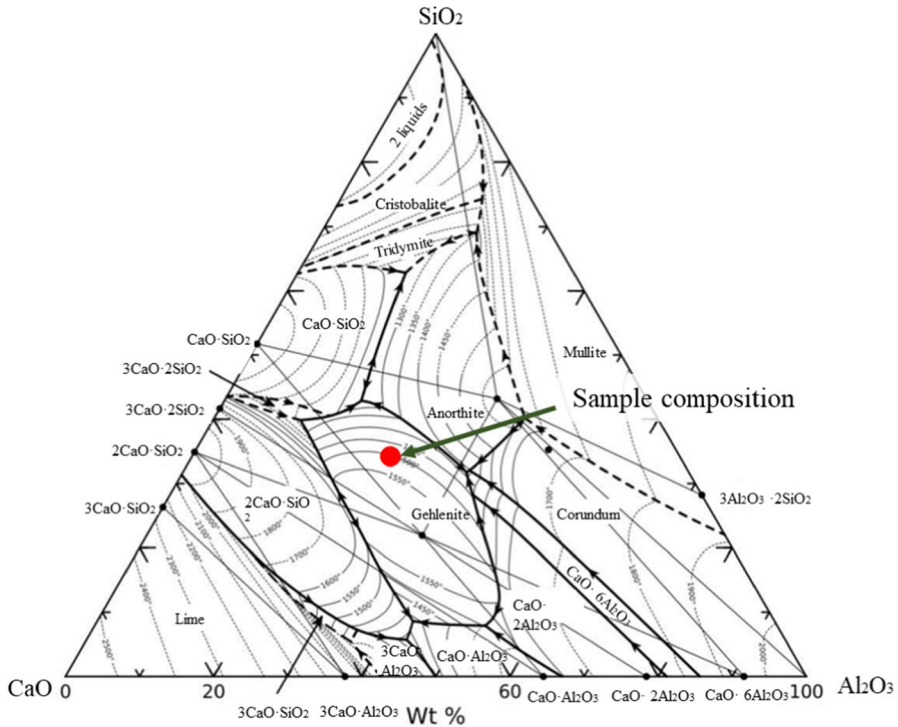


Fig. 1 Phase diagram for $\text{CaO}-\text{Al}_2\text{O}_3-\text{SiO}_2$ system [36]

[35]. CaO was prepared by thermal decomposition of the CaCO_3 reagent and maintained at 1323 K for 720 min. For the sample preparation, the reagent powders were weighed and mixed in an alumina mortar for 30 min. A platinum tube with an inner diameter of 3 mm and a length of 30 mm was used as a crucible; one end of the tube was crushed and rounded to prepare the bottom. The sample mixture was inserted into a crucible and held at 1800 K for 720 min in the air in an electric furnace. The sample was then cooled to 1600 K to enable the crystallization of gehlenite as the primary crystal phase, held for 720 min to coarsen the primary crystals, then cooled to room temperature (293 K).

The samples were then resin-filled in a crucible and mirror-polished. Optical microscopy was used to observe the samples. The mass percentage of the crystallized phase was calculated from the optical microscopy image using the ImageJ software (version 1.51j) [36]. X-ray diffraction (XRD) was used to identify the crystallized phases in the samples, where Co was used as the X-ray source. Measurements were performed in the 2θ range of 10° to 80° .

2.2 Thermal Microscopy

The value of b was measured using a thermal microscope [30]. The measurement area was observed using an optical microscope to determine its correspondence with the microstructure. DC sputtering formed a 125 nm thick Mo film on the sample surface. In the thermal microscopy measurements, a modulated laser with a wavelength of 808 nm, spot diameter of 7 μm , and heating frequency of 1 MHz heated the sample surface. When the laser periodically heats the Mo film, heat penetrates through the Mo film into the sample, and the temperature on the same surface changes at the same frequency as the heating laser. However, there is a phase difference (θ) between the heating laser and the temperature of the sample surface. The value of θ depends on the value of b of the sample through the equation as follows:

$$\theta = \frac{3\pi}{4} + \arctan \left[\frac{\cosh^2 \sqrt{\frac{\omega\tau_f}{2}} \left(\tanh \sqrt{\frac{\omega\tau_f}{2}} + \beta \right) \left(\tanh \sqrt{\frac{\omega\tau_f}{2}} + \beta^{-1} \right)}{\cos^2 \sqrt{\frac{\omega\tau_f}{2}} (\beta - \beta^{-1}) \tan \sqrt{\frac{\omega\tau_f}{2}}} \right], \quad (1)$$

here

$$\tau_f = d_f^2 / \alpha_f, \quad (2)$$

$$\beta = b_s / b_f, \quad (3)$$

where ω , d_f , d_s , b_s , and b_f are the angular frequency of the heating laser, the thickness of Mo film, the thermal diffusivity of Mo film, and values of b for sample and Mo film, respectively. Equation 1 determines the value of β to obtain b_s through Eq. 3. The phase difference (θ) is measured using a detection laser with a wavelength of 633 nm and spot diameter of 3 μm , based on the characteristic that the reflectance of the detection laser changes depending on the surface temperature of the Mo film. An area of $290 \times 290 \mu\text{m}^2$ was measured at 10 μm intervals with 30 times measurements at each position and a waiting time of 10 s.

The value of b of crystallized sample was determined from a calibration curve [32] using standards with the known value of b (Si, Ge, and Pyrex glass). When the value of b is smaller than about $3 \text{ kJs}^{-0.5} \cdot \text{m}^{-2} \cdot \text{K}^{-1}$, thermal microscopy can produce the value of b from the principle expressed as Eq. 1 [29, 30]. For the sample with a larger value of b , the fundamental requirement, i.e., the one-dimensional heat flow, is not satisfied. The calibration curve method is applicable in this case [30, 32, 33]. The relationship between θ and b for the standard samples was used to obtain the calibration curve. The value of b of the sample was determined from θ of the sample. To apply the calibration curve method, the sample and standard samples must have almost the same value of $C\rho$ [32, 33]. In this study, the standard samples used were Si, Ge and Pyrex glass. The values of $C\rho$ for these samples are $1.7 \text{ JK}^{-1} \cdot \text{m}^{-3}$ [32]. The value of b of each standard sample was obtained from the thermal diffusivity (α), specific heat (C), and density (ρ) using the following equations:

$$b = C\rho\sqrt{\alpha}. \quad (4)$$

The values of α , C , and ρ of the standard samples were measured by the laser flash method, differential scanning calorimetry (DSC), and Archimedean method, respectively. To summarize again, the calibration curve can be applied for the sample with the value of b between about $3 \text{ kJs}^{-0.5} \cdot \text{m}^{-2} \cdot \text{K}^{-1}$ and $1.4 \text{ kJs}^{-0.5} \cdot \text{m}^{-2} \cdot \text{K}^{-1}$ (Pyrex) and for the sample having b value between $3 \text{ kJs}^{-0.5} \cdot \text{m}^{-2} \cdot \text{K}^{-1}$ and $15.8 \text{ kJs}^{-0.5} \cdot \text{m}^{-2} \cdot \text{K}^{-1}$ with the limitation of $C\rho = 1.7 \text{ JK}^{-1} \cdot \text{m}^{-3}$.

According to Eq. 1, the thickness of Mo film affects the θ value measurement. Thus, thermal microscopy measurements were conducted for both the standard and main samples under the same conditions. Pyrex glass was used as a sample to examine the validity of the measurements. An area of $300 \times 300 \mu\text{m}^2$ was measured 30 times at $20 \mu\text{m}$ intervals with a measurement latency of 10 s each.

The structure around the measurement position influences the obtained b value. The following equation expresses the thermal diffusion depth (L) of the heating laser:

$$L = \sqrt{\frac{\alpha}{\pi f}} = \frac{b}{\rho C} \sqrt{\frac{1}{\pi f}}, \quad (5)$$

where f is the frequency of the heating laser. The internal microstructure of the sample was confirmed by polishing the sample surface after the measurement.

3 Results and Discussion

3.1 Sample Characterization

Figure 2 shows the appearance of the sample. The sample in the upper part of the crucible was glassy and crystallized in the lower part. Figure 3 shows the XRD

Fig. 2 Appearance of the crystallized sample

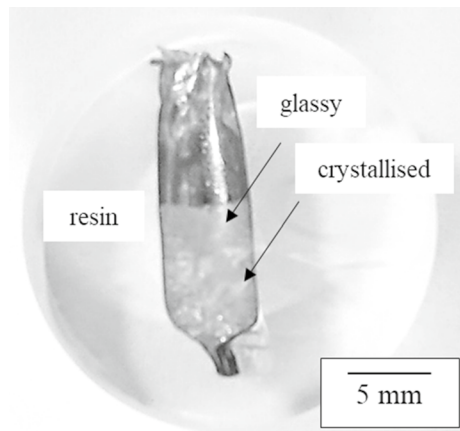
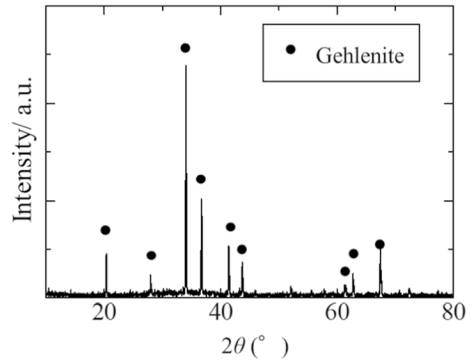


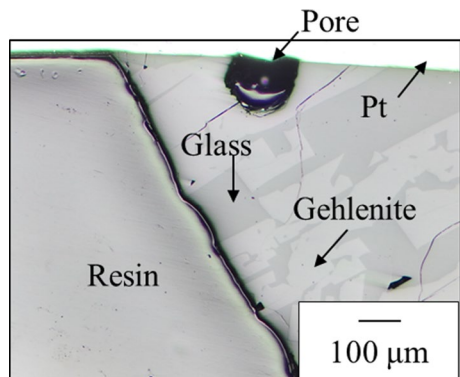
Fig. 3 XRD profiles for sample

result. The identified peaks correspond to gehlenite [37]. Figure 4 shows the microstructure of the sample observed using optical microscopy. The sample has a crystallized phase, which is gehlenite, in the glass matrix. The gehlenite appears to have a faceted structure.

3.2 Thermal Microscopy Results

3.2.1 Pyrex Glass

The results of measurements for the Pyrex glass are shown in Fig. 5a. The measurements were conducted at the grid points in the figure. The maximum b value was $2.3 \text{ kJs}^{-0.5} \cdot \text{m}^{-2} \cdot \text{K}^{-1}$, and the minimum b value was $1.3 \text{ kJs}^{-0.5} \cdot \text{m}^{-2} \cdot \text{K}^{-1}$. Variations in the value of b are shown in Fig. 5b. The number of measurement points was 256, the mean value was $1.52 \text{ kJs}^{-0.5} \cdot \text{m}^{-2} \cdot \text{K}^{-1}$, and the standard deviation was $0.21 \text{ kJs}^{-0.5} \cdot \text{m}^{-2} \cdot \text{K}^{-1}$. Most of the obtained thermal effusivities were between $1.4 \text{ kJs}^{-0.5} \cdot \text{m}^{-2} \cdot \text{K}^{-1}$ and $1.6 \text{ kJs}^{-0.5} \cdot \text{m}^{-2} \cdot \text{K}^{-1}$. The standard value of b used was $1.36 \text{ kJs}^{-0.5} \cdot \text{m}^{-2} \cdot \text{K}^{-1}$ for Pyrex glass, which was determined by the thermal diffusivity, specific heat, and density.

Fig. 4 Optical microscope image of sample

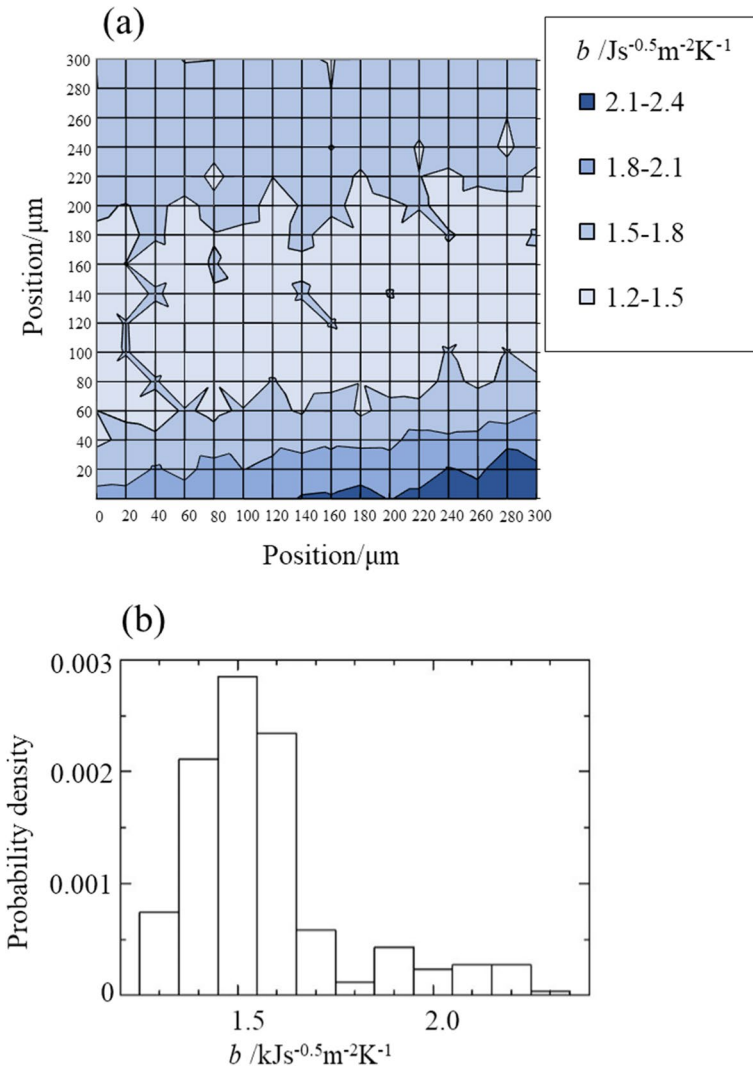


Fig. 5 (a) Distribution of measured value of b for Pyrex glass and (b) probability density against b of Pyrex glass

The uncertainty for the measurement of the b value for Pyrex glass was analyzed according to the guide to the expression of uncertainty in measurement (GUM) [38]. The major sources of uncertainty are measurements of phase delay and thickness of Mo film. The sensitivity coefficient for phase delay was estimated from the calibration curve, whereas that for the thickness of Mo film was estimated based on Eq. 1 under the condition that $d_f = 125$ nm, $\alpha_f = 4.59 \times 10^{-6}$ ($C_{fpf} = 2.29 \times 10^6$ and $\lambda_f = 10.5$ $\text{Wm}^{-1}\cdot\text{K}^{-1}$ [32]) and $b_s = 1.36$ $\text{kJJs}^{-0.5}\text{m}^{-2}\text{K}^{-1}$. The repeatability of phase delay was calculated from the estimated standard deviation of the 30 times

measurements as 0.5° . The accuracy of phase delay measurement was estimated from that the resolution of phase delay was 0.0001° assuming the uniform distribution. The accuracy of the thickness of Mo film was estimated 1 nm, and a uniform distribution was assumed. The thickness of Mo film changes from position to position, which could change 16 nm in an area of $20\ \mu\text{m} \times 20\ \mu\text{m}$ [34], which is the same as the measurement step in the measurement for Pyrex glass. The standard uncertainty was estimated assuming the triangle distribution. In addition, the repeatability of measurement of the b value was also considered based on Fig. 5b. The calibration curve was also the affecting factor. The Pyrex glass used as the standard sample showed a phase delay of 55.7° for $b = 1.36\ \text{kJ s}^{-0.5} \cdot \text{m}^{-2} \cdot \text{K}^{-1}$; however, by inputting the same phase delay into the calibration curve, the obtained value of b was $1.40\ \text{kJ s}^{-0.5} \cdot \text{m}^{-2} \cdot \text{K}^{-1}$. The effect was also considered for the uncertainty. Finally, the combined standard uncertainty for the measurement of b value was calculated to be $0.05\ \text{kJ s}^{-0.5} \cdot \text{m}^{-2} \cdot \text{K}^{-1}$, resulting in $b = 1.5 \pm 0.1\ \text{kJ s}^{-0.5} \cdot \text{m}^{-2} \cdot \text{K}^{-1}$ with the coverage factor $k = 2$.

Thermal conductivity was calculated using the following equation:

$$\lambda = \frac{b^2}{C\rho}. \quad (6)$$

The thermal conductivity for Pyrex glass was calculated to be $1.4 \pm 0.2\ \text{W m}^{-1} \cdot \text{K}^{-1}$, where $\rho = 2218\ \text{kg m}^{-3}$ and $C = 773\ \text{J kg}^{-1} \cdot \text{K}^{-1}$ were used for the calculation [32]).

3.2.2 Crystallized Sample

The measured value of b of the crystallized sample is shown in Fig. 6a. The measurements were taken at the grid points in the figure. Figure 6b shows a photograph of the measurement position observed using an optical microscope. The value of b of the glass part was small, and that of the gehlenite part was large, indicating that the value of b corresponded to the image obtained by optical microscopy. Because the spatial resolution of the laser used to measure the value of b was $3\ \mu\text{m}$, the value of b near the boundary of the glass and gehlenite is between the two phases. The maximum and minimum b values for the gehlenite part were $3.28\ \text{kJ s}^{-0.5} \cdot \text{m}^{-2} \cdot \text{K}^{-1}$ and $1.30\ \text{kJ s}^{-0.5} \cdot \text{m}^{-2} \cdot \text{K}^{-1}$, respectively. The values of b are larger than that of Pyrex glass but smaller than or the same as about $3\ \text{kJ s}^{-0.5} \cdot \text{m}^{-2} \cdot \text{K}^{-1}$. The former suggests that the values of b were in the range of those for the standard samples. And the latter indicates that the calibration curve introduced values of b directly without considering the effect of $C\rho$ of the measured portion; i.e., one-dimensional heat flow was achieved in the measurements.

The thermal diffusion depth in the measurement was calculated to be $0.8\ \mu\text{m}$ from Eq. 5, where $C = 753\ \text{J kg}^{-1} \cdot \text{K}^{-1}$ [39], $\rho = 3038\ \text{kg m}^{-3}$ [37], $f = 1\ \text{MHz}$ and b (maximum value) $= 3.28\ \text{kJ s}^{-0.5} \cdot \text{m}^{-2} \cdot \text{K}^{-1}$ were used. Figure 6c shows a photograph of the microstructure of the sample surface after polishing it to a depth of approximately $7\ \mu\text{m}$, which is greater than the diffusion depth. The

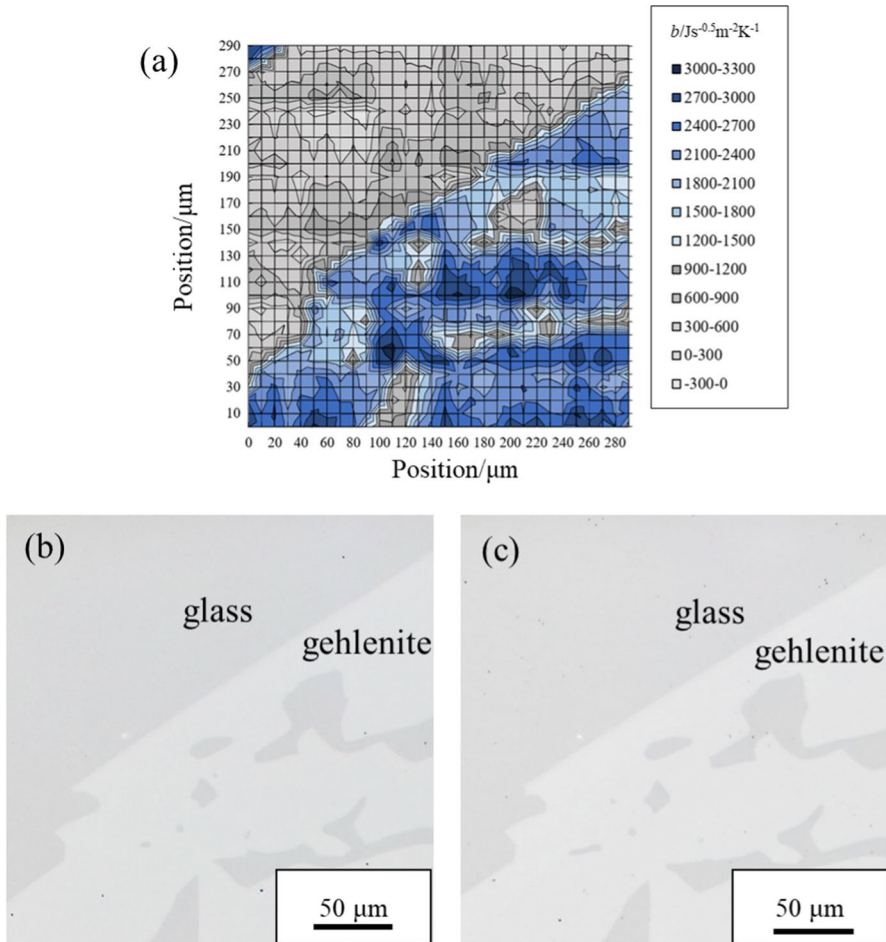
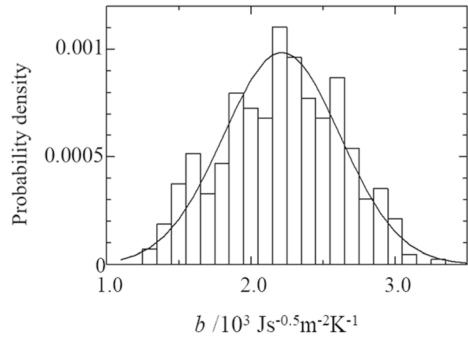


Fig. 6 (a) Distribution of value of b of sample, (b) optical microscope image for measured area and (c) optical microscope images after polishing 7 μm

microstructures before and after polishing showed little difference. It is confirmed that the measured values at the location of gehlenite can be those for gehlenite and are not affected by the glass or grain boundaries. The b value for the gehlenite portion was extracted and shown as a histogram in Fig. 7. The values of b ranged from 1.3 $\text{kJ}_s^{-0.5} \cdot \text{m}^{-2} \cdot \text{K}^{-1}$ to 3.3 $\text{kJ}_s^{-0.5} \cdot \text{m}^{-2} \cdot \text{K}^{-1}$ with 427 measurement points. The obtained value of b of the gehlenite shows a variation similar to that of a normal distribution: an average of 2.2 $\text{kJ}_s^{-0.5} \cdot \text{m}^{-2} \cdot \text{K}^{-1}$ and a standard deviation of 0.4 $\text{kJ}_s^{-0.5} \cdot \text{m}^{-2} \cdot \text{K}^{-1}$. The uncertainty of the measured b value for gehlenite was estimated like for Pyrex glass, as shown in Table 2. The value of b is expressed with the uncertainty as $2.2 \pm 0.1 \text{ kJ}_s^{-0.5} \cdot \text{m}^{-2} \cdot \text{K}^{-1}$ with the coverage factor $k = 2$.

Fig. 7 Probability density of measured value of b for gehlenite



The thermal conductivity of gehlenite was determined to be $2.1 \pm 0.2 \text{ Wm}^{-1} \cdot \text{K}^{-1}$ from $C = 753 \text{ Jkg}^{-1} \cdot \text{K}^{-1}$ [39], $\rho = 3038 \text{ kgm}^{-3}$ [37].

3.3 Comparison with Reported Values

The relationship between the number of oxide components and thermal conductivity is shown in Fig. 8 [40–48]. The states of the crystal grains of each oxide are listed in Table 1 [40–48]. As shown in Fig. 8, the thermal conductivity of the oxides tended to decrease as the number of constituents increased. This is because compared to single-component oxides, composite oxides consisting of two or more components have a more complex crystal structure and poorer symmetry. This results in shorter phonon mean free paths and lower thermal conductivity. Even in oxides of the same composition, differences in thermal conductivity are thought to be due to differences in the metal species and crystal structure that make up the oxides. Gehlenite is composed of three components, CaO , Al_2O_3 , and SiO_2 , and it has a lower thermal conductivity than the constituent components, showing the same trend as in Fig. 8.

There have been two reports on the thermal conductivity of gehlenite. Jia et al. reported thermal conductivities of sintered gehlenite samples—the value was $0.15 \text{ Wm}^{-1} \cdot \text{K}^{-1}$ to $0.25 \text{ Wm}^{-1} \cdot \text{K}^{-1}$ near room temperature [28]. The sample contained many pores, which resulted in a much lower thermal conductivity than

Fig. 8 Thermal conductivity of oxides at 293 K to 329 K

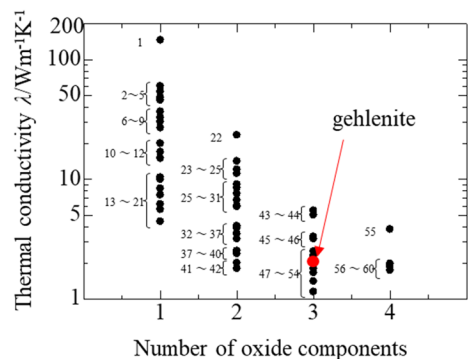


Table 1 Uncertainty budget of the measurement of b value for Pyrex glass

Factor, x_i	Type	Standard uncertainty, $u(x_i)$	Units	Sensitivity coefficient, c_i
Value of b		38.3	$\text{Js}^{-0.5}\cdot\text{m}^{-2}\cdot\text{K}^{-1}$	1
Repeatability	A	13.1	$\text{Js}^{-0.5}\cdot\text{m}^{-2}\cdot\text{K}^{-1}$	
Calibration curve	A	36	$\text{Js}^{-0.5}\cdot\text{m}^{-2}\cdot\text{K}^{-1}$	
Phase delay		0.091	°	93
Repeatability	A	0.091	°	
Accuracy of measurement	B	0.577×10^{-5}	°	
Thickness of Mo film		3.32	nm	8
Accuracy	B	0.577	nm	
Distribution	A	3.27	nm	
Combined standard uncertainty		$u_c(b) = \sqrt{\sum [c_i u(x_i)]^2} = 54.7 \text{ Js}^{-0.5}\cdot\text{m}^{-2}\cdot\text{K}^{-1}$		

that obtained in this study. Steadman et al. reported the thermal conductivities of sintered samples with compositions of $\text{SiO}_2\text{-Al}_2\text{O}_3\text{-CaO-Fe}_2\text{O}_3\text{-MgO-Na}_2\text{O}$. The main phase of the sample was gehlenite with values of $0.9 \text{ Wm}^{-1}\cdot\text{K}^{-1}$ to $1.3 \text{ Wm}^{-1}\cdot\text{K}^{-1}$ [27]. The density of the sample was reported to be 3039 kgm^{-3} to 3054 kgm^{-3} , which is almost the same as that for a single crystal of gehlenite (3038 kgm^{-3} [37]). Even the dense sample showed higher thermal conductivity; the densest sample reported by Steadman et al. had a smaller value than that in this study. The difference could be due to the impurity of the sample; the sample used by Steadman et al. contained Fe_2O_3 , MgO , and Na_2O in addition to the constituents of gehlenite. Considering the steelmaking process, it is possible that impurities may be present in gehlenite. This indicates that it is necessary to study

Table 2 Uncertainty budget of the measurement of b value for gehlenite

Factor, x_i	Type	Standard uncertainty, $u(x_i)$	Units	Sensitivity coefficient, c_i
Value of b		40.9	$\text{Js}^{-0.5}\cdot\text{m}^{-2}\cdot\text{K}^{-1}$	1
Repeatability	A	19.4	$\text{Js}^{-0.5}\cdot\text{m}^{-2}\cdot\text{K}^{-1}$	
Calibration curve	A	36	$\text{Js}^{-0.5}\cdot\text{m}^{-2}\cdot\text{K}^{-1}$	
Phase delay		0.086	°	328
Repeatability	A	0.086	°	
Accuracy of measurement	B	0.577×10^{-5}	°	
Thickness of Mo film		3.32	nm	10
Accuracy	B	0.577	nm	
Distribution	A	3.27	nm	
Combined standard uncertainty		$u_c(b) = \sqrt{\sum [c_i u(x_i)]^2} = 59.7 \text{ Js}^{-0.5}\cdot\text{m}^{-2}\cdot\text{K}^{-1}$		

Table 3 Oxides and sample conditions compared in this study

Number	Oxide	Purity	Porosity	Crystal condition
1	BeO	99.50 %	2 %	
2	MgO	99.96 %	0 %	Single crystal
3	ZnO		0 %	Single crystal//C
4	MgO	99.50 %	2 %	
5	Al ₂ O ₃		0 %	Single crystal, 60° from <i>h</i> -axis
6	NiO			Single crystal
7	Al ₂ O ₃	99.5 %~		
8	SnO ₂	98 %		
9	Y ₂ O ₃		0 %	Single crystal
10	β-Ga ₂ O ₃			Single crystal, 【010】
11	CaO		8.75 %	
12	Fe ₂ O ₃			Sintered
13	SiO ₂	High	0 %	Single crystal//C
14	TiO ₂	99.997 %	0 %	Single crystal//C
15	FeO			Sintered
16	MnO			Single crystal
17	TiO ₂	99.50 %	2 %	
18	TiO ₂	99.997 %	0 %	Single crystalLC
19	SiO ₂	High	0 %	Single crystalLC
20	Cu ₂ O	99.96 %	0 %	Single crystal
21	Fe ₃ O ₄			Single crystal
22	Al ₂ MgO ₄		0 %	Single crystal
23	Al ₂ SiO ₅ (Kyanite)			
24	Al ₅ Y ₃ O ₁₂			Single crystal
25	SrTiO ₃		0%	Single crystal
26	Al ₂ SiO ₅ (Sillimanite)			
27	Mg ₂ SiO ₄		4.40 %	
28	Al ₂ SiO ₅ (Andalusite)			
29	MgSiO ₃		3.20 %	
31	Al ₆ Si ₂ O ₁₃		11.40 %	
32	CdCr ₂ O ₄			Polycrystal
33	CaSiO ₃			
34	SiZrO ₄			Single crystal
35	K ₂ Ti ₆ O ₁₃	99.9 %~	2.20 %	
36	MoSrO ₄			Sintered
37	Fe ₂ SiO ₄			Sintered
38	Cr ₂ FeO ₄			
39	Cr ₂ MgO ₄			Polycrystal
40	Cr ₂ ZnO ₄			Polycrystal
41	BaMoO ₄			Sintered
42	BaTiO ₃		3.40 %	
43	Al ₂ Ca ₃ Si ₃ O ₁₂			

Table 3 (continued)

Number	Oxide	Purity	Porosity	Crystal condition
44	CaMgSi ₂ O ₆			
45	Al ₂ Fe ₃ Si ₃ O ₁₂			
46	Al ₂ Mg ₃ Si ₃ O ₁₂			
47	AlKSi ₃ O ₈ (Microcline)			
48	AlKSi ₃ O ₈ (Orthoclase)			
49	Ca ₅ Mg ₄ V ₆ O ₂₄			Single crystal
50	Ca ₅ Zn ₄ V ₆ O ₂₄			Single crystal
51	Ca ₂ Ga ₂ SiO ₇			Single crystal (Nd ³⁺ doped), <i>a</i> -axis
52	AlKSi ₃ O ₈ (Sanidine)			
53	Ca ₂ Ga ₂ SiO ₇			Single crystal (Nd ³⁺ doped), <i>c</i> -axis
54	AlKSi ₂ O ₆			
55	CaFeMgSi ₃ O ₉			
56	Ca ₅ Co ₂ Mg ₂ V ₆ O ₂₄			Single crystal
57	Ca ₅ MgV ₆ Zn ₃ O ₂₄			Single crystal
58	Ca ₅ Mg ₃ V ₆ ZnO ₂₄			Single crystal
59	Ca ₅ Mg ₂ V ₆ Zn ₂ O ₂₄			Single crystal
60	Al ₄ KNa ₃ Si ₄ O ₁₆			

the thermal conductivity after clarifying the composition of gehlenite in the mold flux after its use in actual equipment (Tables 2 and 3).

4 Conclusions

Using thermal microscopy, the value of $\sqrt{\lambda C \rho}$ of a gehlenite sample was measured at room temperature to be $2.2 \pm 0.1 \text{ kJs}^{-0.5} \cdot \text{m}^{-2} \cdot \text{K}^{-1}$, producing a thermal conductivity of $2.1 \pm 0.2 \text{ Wm}^{-1} \cdot \text{K}^{-1}$. The thermal conductivity of gehlenite was smaller than that of its constituent components, i.e., CaO, Al₂O₃ and SiO₂. The low thermal conductivity was comparable to that of other composite oxides comprising these three components.

Acknowledgements The authors would like to thank Bethel Co., Ltd. for the measurements using thermal microscopy and the useful discussion of the results. We would like to thank Editage (www.editage.com) for English language editing.

Author Contributions RE conceived and planned the experiments. TW decided on the experimental conditions. YI performed the measurements and analysis. MH and MS helped supervise YI YI and RE wrote the main manuscript text. All authors discussed the results and contributed to the final manuscript.

Funding This research did not receive any specific grant from funding agencies in the public, commercial, or not-for-profit sectors.

Declarations

Competing interest The authors have no conflicts of interest to declare that are relevant to the content of this article.

Ethical Approval Not applicable.

Open Access This article is licensed under a Creative Commons Attribution 4.0 International License, which permits use, sharing, adaptation, distribution and reproduction in any medium or format, as long as you give appropriate credit to the original author(s) and the source, provide a link to the Creative Commons licence, and indicate if changes were made. The images or other third party material in this article are included in the article's Creative Commons licence, unless indicated otherwise in a credit line to the material. If material is not included in the article's Creative Commons licence and your intended use is not permitted by statutory regulation or exceeds the permitted use, you will need to obtain permission directly from the copyright holder. To view a copy of this licence, visit <http://creativecommons.org/licenses/by/4.0/>.

References

1. H. Nakada, M. Susa, Y. Seko, M. Hayashi, K. Nagata, *ISIJ Int.* **48**, 446–453 (2008). <https://doi.org/10.2355/isijinternational.48.446>
2. S. Ozawa, M. Susa, T. Goto, R. Endo, K.C. Mills, *ISIJ Int.* **46**, 413–419 (2006). <https://doi.org/10.2355/isijinternational.46.413>
3. M. Hanao, M. Kawamoto, M. Hara, T. Murakami, H. Kikuchi, K. Hanazaki, *Tetsu-to-Hagané* **88**, 23–28 (2002). https://doi.org/10.2355/tetsutohagane1955.88.1_23
4. R. Endo, Y. Kono, Y. Kobayashi, M. Susa, S. Mineta, H. Yamamura, *Tetsu-to-Hagane*. **100**, 571–580 (2014). <https://doi.org/10.2355/tetsutohagane.100.571>
5. M. Hanao, M. Kawamoto, T. Watanabe, *ISIJ Int.* **44**, 827–835 (2004). <https://doi.org/10.2355/isijinternational.44.827>
6. H. Nakada, H. Fukuyama, K. Nagata, *ISIJ Int.* **46**, 1660–1667 (2006). <https://doi.org/10.2355/isijinternational.46.1660>
7. J. Li, B. Yan, Q. Shu, K. Chou, *Metall. Mater. Trans. B* **46**, 2458–2469 (2015). <https://doi.org/10.1007/s11663-015-0422-y>
8. H. Mizuno, H. Esaka, K. Shinozuka, M. Tamura, *ISIJ Int.* **48**, 277–285 (2008). <https://doi.org/10.2355/isijinternational.48.277>
9. X. Long, Q. Wang, S. He, P.C. Pistorius, *Metall. Mater. Trans. B* **48**, 1938–1942 (2017). <https://doi.org/10.1007/s11663-017-1004-y>
10. A. Cruz, F. Chávez, A. Romero, E. Palacios, V. Arredondo, *J. Mater. Process. Technol.* **182**, 358–362 (2007). <https://doi.org/10.1016/j.jmatprotec.2006.08.015>
11. J. Guo, M.D. Seo, C.B. Shi, J.W. Cho, S.H. Kim, *Metall. Mater. Trans. B* **47**, 2211–2221 (2016). <https://doi.org/10.1007/s11663-016-0697-7>
12. M.D. Seo, C.B. Shi, J.Y. Baek, J.W. Cho, S.H. Kim, *Metall. Mater. Trans. B* **46**, 2374–2383 (2015). <https://doi.org/10.1007/s11663-015-0358-2>
13. J. Yang, M. Zhu, *ISIJ Int.* **56**, 2191–2198 (2016). <https://doi.org/10.2355/isijinternational.ISIJINT-2016-315>
14. M. Hayashi, T. Watanabe, H. Nakada, K. Nagata, *ISIJ Int.* **46**, 1805–1809 (2006). <https://doi.org/10.2355/isijinternational.46.1805>
15. W. Wang, K. Blazek, A. Cramb, *Metall. Mater. Trans. B* **39**, 66–74 (2008). <https://doi.org/10.1007/s11663-007-9110-x>
16. H. Ohta, H. Shibata, T. Emi, Y. Waseda, *J. Jpn. Inst. Met.* **61**, 350–357 (1997). https://doi.org/10.2320/jinstmet1952.61.4_350
17. Z.T. Zhang, G.H. Wen, J.L. Liao, S. Sridhar, *Steel Res. Int.* **81**, 516–528 (2010). <https://doi.org/10.1002/srin.201000058>
18. W. Wang, K. Gu, L. Zhou, F. Ma, I. Sohn, D.J. Min, H. Matsuura, F. Tsukihashi, *ISIJ Int.* **51**, 1838–1845 (2011). <https://doi.org/10.2355/isijinternational.51.1838>

19. J. Chen, F. He, Y. Xiao, M. Xie, J. Xie, W. Zhang, J. Shi, *Constr. Build. Mater.* **216**, 19–28 (2019). <https://doi.org/10.1016/j.conbuildmat.2019.04.261>
20. L. Zhou, W. Wang, K. Zhou, *Metall. Mater. Trans. E* **2**, 99–108 (2015). <https://doi.org/10.1007/s40553-015-0047-8>
21. M. Susa, K. Sasaki, T. Yamauchi, T. Watanabe, R. Endo, M. Hayashi, M. Hanao, *ISIJ Int.* **60**, 58–64 (2020). <https://doi.org/10.2355/isijinternational.ISIJINT-2019-266>
22. Z. Wang, I. Sohn, *ISIJ Int.* **60**, 2705–2716 (2020). <https://doi.org/10.2355/isijinternational.ISIJNT-2019-522>
23. K.C. Mills, *ISIJ Int.* **56**, 14–23 (2016). <https://doi.org/10.2355/isijinternational.ISIJINT-2015-355>
24. W. Yan, W. Chen, Y. Yang, C. Lippold, A. Mclean, *ISIJ Int.* **55**, 1000–1009 (2015). <https://doi.org/10.2355/isijinternational.55.1000>
25. M. Persson, M. Görnerup, S. Seetharaman, *ISIJ Int.* **47**, 1533–1540 (2007). <https://doi.org/10.2355/isijinternational.47.1533>
26. V. Kircher, I. Marschall, N. Kölbl, H. Harmuth, *Proc. 8th European Continuous Casting Conf. (ASMET, Leoben, Austria, 2014)*, p. 1050
27. E. N. Steadman, S. A. Benson, J. W. Nowok, *Twelfth Annual Gasification and Gas Stream Cleanup Contractors Review Meeting (National Technical Information Service, Springfield, 1992)*, p. 279. <https://doi.org/10.2172/10110104>
28. D. Jia, D.K. Kim, W.M. Kriven, *J. Am. Ceram. Soc.* **90**, 1760–1773 (2007). <https://doi.org/10.1111/j.1551-2916.2007.01704.x>
29. K. Hatori, N. Taketoshi, T. Baba, H. Ohta, *Rev. Sci. Instrum.* **76**, 114901 (2005). <https://doi.org/10.1063/1.2130333>
30. K. Hatori, H. Ohta, *Netsu Bussei.* **22**, 84–91 (2008). <https://doi.org/10.2963/jjtp.22.84>
31. Y. Okamoto, R. Okada, T. Nemoto, H. Ohta, H. Takiguchi, *Int. J. Thermophys.* **33**, 1219–1227 (2012). <https://doi.org/10.1007/s10765-012-1249-2>
32. H. Ohta, K. Hatori, G. Matsui, T. Yagi, S. Miyake, T. Okamura, R. Endoh, R. Okada, K. Morishita, S. Yokoyama, K. Taguchi, H. Kato, *Meas. Sci. Technol.* **27**, 115002 (2016). <https://doi.org/10.1088/0957-0233/27/11/115002>
33. S. Miyake, G. Matsui, H. Ohta, K. Hatori, K. Taguchi, S. Yamamoto, *Meas. Sci. Technol.* (2017). <https://doi.org/10.1088/1361-6501/aa72d0>
34. T. Nishi, S. Yamamoto, M. Okawa, K. Hatori, T. Ikeda, H. Ohta, *Thermochim. Acta* **659**, 39 (2018). <https://doi.org/10.1016/j.tca.2017.11.004>
35. E. Haccuria, T. Crivits, P.C. Hayes, E. Jak, *J. Am. Ceram. Soc.* **99**, 691–704 (2016). <https://doi.org/10.1111/jace.13991>
36. M.D. Abramoff, P.J. Magalhães, S.J. Ram, *Biophotonics Int.* **11**, 36 (2004)
37. E. Osborn, *Am. Mineral.* **34**, 717 (1949)
38. ISO/IEC Guide 98 (1995).
39. I. Barin, *Thermochemical Data of Pure Substances*, 3 (VCH Verlagsgesellschaft mbH, Weinheim, 1995), p.448
40. Y. Touloukian, R. Powell, C. Ho, P. Klemens, *Thermal Conductivity Nonmetallic Solids*, vol. 2 (Plenum Press, New York, 1970), p.98
41. M. Takeda, T. Onishi, S. Nakakubo, S. Fujimoto, *Mater. Trans.* **50**, 2242–2246 (2009). <https://doi.org/10.2320/matertrans.M2009097>
42. K. Kurosaki, K. Tanaka, M. Osaka, K. Tokushima, H. Gima, H. Muta, M. Uno, S. Yamanaka, *Trans. Nihon Genshiryoku Gakkai Wabun Rombunshi.* **9**, 21–28 (2010). <https://doi.org/10.3327/taesj.J09.001>
43. A.S. Tolkacheva, P.A. Popov, S.N. Shkerin, S.V. Naumov, P.D. Khavlyuk, A.A. Krugoviykh, S.V. Telgin, *Russ. J. Appl. Chem.* **93**, 325–332 (2020). <https://doi.org/10.1134/S1070427220030027>
44. C. Shen, D. Wang, H. Xu, Z. Pan, H. Zhang, J. Wang, R.I. Boughton, *J. Alloys Compd.* **727**, 8–13 (2017). <https://doi.org/10.1016/j.jallcom.2017.07.217>
45. Japan Society of Thermophysical Properties, *Thermophysical Properties Handbook*, Youkendo, Tokyo, vol. 291, (2008)
46. V. Cermak, L. Rybach, *Thermal Properties, Thermal Conductivity and Specific Heat of Minerals and Rocks*, vol. 305 (Springer, Berlin, 1982)
47. H.D. Zhou, Z.Y. Zhao, X.F. Sun, M.N. Suarez, B. Rivas-Murias, V. Tsurkan, J. Deisenhofer, V.S. Zapf, F. Rivadulla, *Phys. Rev. B* **87**, 174436 (2013). <https://doi.org/10.1103/PhysRevB.87.174436>
48. P. Jiang, X. Qian, X. Li, R. Yang, *Appl. Phys. Lett.* **113**, 232105 (2018). <https://doi.org/10.1063/1.5054573>

Publisher's Note Springer Nature remains neutral with regard to jurisdictional claims in published maps and institutional affiliations.